# The influence of heating rate on W-Cr-Zr alloy densification process and microstructure evolution during spark plasma sintering

*W.J. Wang[a†], X.Y. Tan[a,b†], J.Q. Liu[c], X. Chen[c], M. Wu[a], L.M. Luo[a], X.Y. Zhu[d], H.Y. Chen[e], Y.R. Mao[a,b], A. Litnovsky[b], J.W. Coenen[b], Ch.Linsmeier[b], Y.C. Wu[a,c,d]*

*[a]School of Materials Science and Engineering, Hefei University of Technology, Hefei 230009, China; [b]Forschungszenturn Juelich GmbH, Institut fuer Energie- und Klimaforschung – Plasmaphysik, Partner of the Trilateral Euregio Cluster (TEC), Juelich 52425, Germany; [c]Industry & Equipment Technology, Hefei University of Technology, Hefei 230009, China; [d]National-Local Joint Engineering Research Centre of Nonferrous Metals and Processing Technology, Hefei 230009, China; [e]Key Laboratory of E&M (Zhejiang University of Technology), Ministry of Education & Zhejiang Province, Hangzhou 310014, China*

**Abstract:** In this work, the influence of heating rate on the densification process and microstructure evolution of W-Cr-Zr mechanically alloyed powder during spark plasma sintering were investigated. Varying the heating rates from 50 °C/min to 300 °C/min, founding that the W-Cr-Zr samples have a similar relative density after densification. The microstructure evolutions of W-Cr-Zr samples were evaluated, indicating that it could be easier to achieve the homogenous microstructure at a high heating rate. High heating rate means high thermal inertia that lead to the actual temperature of W-Cr-Zr alloys approach or even exceed its solution temperature. The densification process of W-Cr-Zr samples were analyzed by the displacement curves, founding that their densification temperatures are approximately 1380 °C and the high heating rate could promote the densification rate. Notably, the higher the heating rate, the higher the current. High current contributes to decrease sintering activation energy and improve densification process.

**Keywords:** First wall; Self-passivating tungsten alloy; W-Cr-Zr alloy; Densification process; Microstructure evolution.

## 1. Introduction

Tungsten (W) is considered to be one of the most promising candidate materials for the first wall in a future fusion power plant, because of its advantages such as high melting point, excellent thermal conductivity, high sputtering threshold and low tritium retention[1,2]. However, the first wall may face a potential loss-of-coolant accident (LOCA) with simultaneous air ingress into the vacuum vessel. Under this situation, the temperature of the first wall would reach up to 1000 °C after ~10 days due to the nuclear decay heat of the in-chamber components[3]. Air ingress leads to the oxidation of the neutron-irradiated W and the formation of volatile oxides[4]. This would result in the sublimation of several hundred $kg \cdot h^{-1}$ of neutron activated $WO_3$ and then may leak into the atmosphere[5]. To avoid this nuclear leakage accident, self-passivating tungsten alloys (SPTAs) were proposed to prevent the formation and sublimation of the highly radioactive oxides by forming a dense oxide layer on the top surface. In case of the normal operation, the surface of SPTAs will be a pure W layer, owing to the preferential sputtering of alloying elements[6].

During the last years, significant efforts were carried out in SPTAs thin film systems, such as W-Cr-Ti[7] ,W-Cr-Y[8] and W-Cr-Si[9] (chromium Cr; yttrium Y; titanium Ti; silicon Si). The addition of Cr, Y, Si or Ti as alloying elements could reduce of the oxidation rate of SPTAs by several orders of magnitude at temperature up to 1000 °C compared to pure W[7-9]. Recently, Tan et al.[10] produced W-Cr-Zr thin film alloy by magnetron sputtering technique, founding that zirconium (Zr) instead of Y in SPTA thin film system can significantly improve the oxidation resistance under an oxidation atmosphere of Ar+20 vol.% $O_2$ at 1000 °C. However, thin film system served as “model materials” was always used to optimize its composition for bulk system[11]. Because of the limited thickness does not allow thin film SPTAs service a long exposure time. Therefore, SPTAs bulk system are being researched and developed for further fusion engineering application. Actually, SPTAs bulk have been manufactured by mechanical alloying (MA) and subsequent hot isostatic pressing (HIP)[6,12] or spark plasma sintering (SPS)[13-15]. A. Calvo et al.[6] reported that highly dense and fine-grained W-Cr-Y alloys

bulk could be obtained by MA and following HIP (1250 °C for 2 h) technique. But it showed an inhomogeneous microstructure with two main phases. In order to obtain a homogenous microstructure with a single-phase, the bulk alloy was heat treated at 1550 °C for 2 h under $H_2$ atmosphere, however, the grain growth is inevitable (from 110 nm to 230 nm)[16]. Based on the current understanding and the previous work[15], SPTAs bulk with high density, fine-grain and homogeneous structures would have an excellent oxidation resistance. But for the densification technique of HIP, it would be impossible to obtain the idea structure of SPTAs. SPS is an advanced densification technique assisted with pressure and current that has garnered widespread popularity in the field of powder metallurgy[17-19]. Essentially, SPS densification technique involves multi-mechanism coupling of localized heating, Joule heating and surface cleaning, which could accelerate powder densification at a low temperature[20,21]. Due to its shorter cycle time, the grain growth was limited and/or controlled. Therefore, it would be possible to manufacture high dense and fine-grained STPA bulks at lower temperature as compared to the other pressure assisted sintering techniques of hot pressing (HP) or HIP. For the SPS densification process, the most essential sintering parameters would contain the sintering temperature, heating rate, holding time and assisted pressure even vacuum. Although many studies have tried to clear the influences of SPS sintering parameters on the densification process of the various W-Cr alloy systems as listed in Table 1[13,15,22]. In the SPS densification of W-11.4Cr-0.6Y alloys[15], founding that increasing sintering temperature or prolonging holding time will result in grain growth. But there is still no systematic research or conclusion on this research topic.

In the present work, we would like to clear how does the heating rate influences on the densification process and the microstructure evolution of W-Cr-Zr alloy. The densification process of W-Cr-Zr samples sintered with different heating rates are mainly analyzed by combining the relative density and instantaneous densification rate. For the influences of heating rate on the microstructure evolutions, different perspectives of grain size, phase composition, dislocation density and hardness are

presented herein.

## 2. Material preparation and characterization

### 2.1 W-Cr-Zr alloyed powder preparation

Elemental powders of pure W (99.9%, 5 μm), Cr (99.9%, 74 μm) and $ZrH_2$ (99.9%, 74 μm) were used as raw materials. Starting powders with nominal composition of W-11.4Cr-1.0Zr (all compositions are represented in wt. % unless specified) were ball-milled in a planetary mill for 80 h in argon atmosphere. The content of Zr was calculated by stoichiometry based on the $ZrH_2$. The $ZrH_2$ would become Zr at the milling stage and the subsequent SPS densification stage. The milling parameters of the rotation speed and the ball-to-powder weight ratio were 225 rpm and 5:1, respectively. In order to minimize the possible impurity contamination, tungsten carbide balls and mortars were used.

### 2.2 W-Cr-Zr bulk densification

The consolidation of the W-Cr-Zr alloyed powder were carried out by SPS (Labox-350, Sinter land inc, Japan) technique, the combination schematic diagram of sintered bulk and graphite die as shown in Fig. 1. The graphite die with an inner diameter of 20 mm was applied to pack the milled powder for the preparation of samples. To prevent the carbon reacts with W-Cr-Zr alloy during the SPS densification process, a molybdenum foil was placed in the inner surface of the graphite die. Before sintering, the vacuum chamber of SPS facility was pumped firstly to below 10 Pa and the green compact was loaded with a pressure of 10 MPa. To study the influences of heating rate, one of samples was sintered at 1500 °C with a different heating rates of 50 °C/min, 100 °C/min, 200 °C/min and 300 °C/min and without holding time. Notably, the temperature at 600 °C was kept for 5 min during the heating stage. Meanwhile, the pressure was evenly loaded from 10 MPa to 50 MPa at the last 2 min. The temperature changes during the SPS densification process was detected by an optical pyrometer. The detection window of the optical pyrometer ranges from 570 °C to 2000 °C. It should be point out that the temperature measuring position is 5 mm from the edge of the

sample in the graphite die, which as marked with “detection point” in Fig. 1. For analyzing the densification process and microstructure evolution of W-Cr-Zr samples, the changes of temperature, displacement, current, pressure and vacuum were recorded in 5 s by the own software system of SPS facility. The displacement change during SPS densification process includes not only the shrink densification of the powder, but also the thermal expansion of the graphite punches. Therefore, it would be necessary to take the thermal expansion of graphite punches into account. To achieve this target, a blank heating cycle was performed on an empty graphite die to understand graphite punches expansion behavior. The SPS process for the empty graphite die is the same with the case for W-Cr-Zr alloy, which was placed in the SPS facility and heated up to 1500 °C with a heating rate of 200 °C/min.

2.3 Characterization

Microstructure or composition changes of the milled powder and sintered bulks were characterized using field emission scanning electron microscopy (FESEM, Sigme Sigma Zeiss, Germany) and the equipped Energy Dispersive X-ray spectrometry (EDX). The specimens for SEM characterization were firstly grinded using SiC papers with different grades and following polished by diamond paste with a particle size of 0.5 μm. Notably, to obtain a higher quality surface, the detected cross section of the W-Cr-Zr milled powder and W-Cr-Zr bulks were thinned by ion beam thinning technique (MODEL-691, Gatan, USA). To clear the phase composition or estimate the microstrain of the powders or bulks, the X-ray diffraction (X'Pert PRO MPD, PANalytical B.V) was carried out from 30° to 90° using Cu K$\alpha$ radiation operating at 40 kV and 40 mA at a scan speed of 6 °/min. The relative density is defined as the ratio of the actual density and the theoretical density. The actual density of the W-Cr-Zr bulk samples were measured by Achimedes’ principle. The theoretical density is simply considered based on the volume fraction and the corresponding theoretical density of each component according to the mixing rules. For the W-Cr-Zr alloy, the theoretical density of W, Cr and Zr components were taken as 19.25 g/cm$^3$, 7.19 g/cm$^3$ and 6.52 g/cm$^3$, respectively. After calculation, the theoretical density of W-11.4Cr-1.0Zr alloy is 15.87

g/cm$^3$. The diameters of grains and nano-precipitates for each sample were measured by the intercept method based on the SEM images containing at least 300 grains. Furthermore, the hardness of the sintered W-Cr-Zr samples were also measured using Vickers hardness tester (Vickers 402 MD, Wilson hardness, China) at a load of 10 kg and dwelling for 15 s. To reduce random error, the final hardness value is taken the averaged from ten out of twelve readings by omitting the maximum and minimum values.

## 3 Results

### 3.1 W-Cr-Zr alloyed powder

The phase composition of raw powders and the milled W-Cr-Zr powders were examined by XRD and the corresponding spectra are showed in Fig. 2a. From the Fig. 2a, the milled W-Cr-Zr powder mainly show a single-phase structure with body-centred cubic (bcc) structure, which means that the milled powders may have achieved a completely solid solution structure. The diffraction peak (110) of W-Cr-Zr powders shows an obvious broadening, which could be due to crystalline refinement and induced lattice strain during MA[24]. In addition, the position of the diffraction peak (110) of W-Cr-Zr powders locates at 41.22°, which shifts the right as compared to that of the pure W (40.26°). Notably, the single-phase peaks could not be a convincing evidence to judge that Cr is completely dissolved in W because of the detection limit of the XRD detector. Fig. 2b shows the morphology of the W-Cr-Zr powders after MA, finding that the powder particles are close to spherical and the particles size with bimodal distribution are less than 10 μm, which would have good powder flowability. To obtain a stronger evidence for verifying the milled powders become completely solid solution, a cross section image of the W-Cr-Zr particles was performed by SEM as shown in Fig. 2c. There is no any obvious singular structure, which is an intuitively evidence supporting that the W-Cr-Zr powders possesses a homogenous structure. Based on the results of XRD spectra and SEM cross section image of the W-Cr-Zr powders, indicating that a completely solid solution of the milled powders has been obtained after 80 h of continuous milling. Previous study has suggested that the preparation of

homogeneous structure of SPTAs powders is considered to be a vital step for producing homogeneous structure of SPTAs[15].

3.2 W-Cr-Zr bulk

After SPS densification at 1500 °C with different heating rates, the microstructures of W-Cr-Zr alloys are characterized by SEM. Fig. 3a shows the microstructure of the W-Cr-Zr sample sintered with a heating rate of 50 °C/min, finding it consists three phases of bright grey majority grains, dark grey discontinuous grains and nano-precipitates. Based on the EDX detection, the three phases would be the W matrix phase, Cr-rich phase and Zr-containing phase, respectively. When the heating rate increased (100 ~ 300 °C/min), it is hard to find out the large sized Cr-rich phases from the microstructures of W-Cr-Zr samples as show in Fig. 3b-3d. These samples show a homogeneous structure with W-matrix phase and dispersed nano-precipitates.

In order to clear the influences of the heating rate on the microstructure of W-Cr-Zr alloy after SPS densification, the phase composition of the W-Cr-Zr samples were examined by XRD. Fig. 4a is the corresponding XRD spectra and shows a bcc structure. Notably, the XRD spectra of the sample sintered with a heating rate of 50 °C/min has a weak peak near the diffraction peak (110), which should be one of diffraction peak of the Cr-rich phase. When the heating rate was above 100 °C/min, the weak peak is hard to detect from the XRD spectra of W-Cr-Zr samples and showing a single-phase bcc structure. Fig. 4b shows the magnified diffraction peak (110) of W-Cr-Zr samples. The gray dotted line is the position of the diffraction peak (110) of W-Cr-Zr alloyed powder (41.22°). It can be found that the diffraction peak (110) of W-Cr-Zr samples have deviated from that of W-Cr-Zr alloyed powder. The offset to the left of the diffraction peak (110) is 0.16 ° if the W-Cr-Zr sample sintered with 50 °C/min, which may be attributed to the severe Cr precipitation. When the W-Cr-Zr sample sintered with a heating rate of 300 °C/min, the offset to the left of the (111) peak is only 0.02 °, i.e., the position of (111) peak is very close to that of (110) peak of W-Cr-Zr alloyed powder. It indicates that the W-Cr-Zr sample sintered with a high heating rate can achieve a completely solid solution structure.

To deeply understand the influence of the heating rate on the microstructure evolution during SPS densification W-Cr-Zr samples by evaluating the evolution of Cr content in the W matrix and hardness. Fig. 5a shows the Cr content in W matrix, which detected by EDX. It is obvious that the Cr content in W matrix increases with the increase of heating rate. When the heating rate is 50 °C/min, the Cr content in the W matrix is approximately 8.9 wt.%, which is consistent with the formation of Cr-rich phase in Fig. 3a. For the case of the heating rate reach up to 300 °C/min, the Cr content in the W matrix is approximately 11.0 wt.%, which is very close to the designated content (11.4 wt.%). The results would be also support that increasing the heating rate during SPS densification process can be benefit to the formation of completely solid solution of W-Cr-Zr alloy. Fig. 5b presents the hardness of the W-Cr-Zr samples sintered at 1500 °C with different heating rate. It shows only a moderate increase as increasing the heating rate from 50 °C/min to 300 °C/min. For the W-Cr-Zr alloy, the main influence factors of hardness could include density, grain size of W matrix, the size and distribution of precipitation phase, and solid solubility. The relative density of W-Cr-Zr alloys sintered with different heating rates were measured by Achimedes' principle and are approximately 98.5%. Based on the SEM images of Fig. 3, the sizes of W-matrix and the nano-precipitates were measured as shown in Fig. 5c and Fig. 5d, respectively. The corresponding sizes are approximately 500 and 50 nm, respectively. In addition, the nano-precipitates are mainly dispersed at the grain boundaries as seen from the current SEM images. Therefore, the hardness difference among of W-Cr-Zr alloys sintered with different heating rates should be attributed to the Cr solubility in the W matrix.

## 4 **Discussions**

### 4.1 Expansion behavior of graphite

During the SPS process, the densification process of the W-Cr-Zr alloyed powder can be analyzed from the curves of displacement change. In order to clear the densification process from the curves of displacement change, the thermal expansion of the graphite punches during the SPS heating stage should be calculated firstly.

When a blank SPS heating cycle performing on an empty graphite die, the applied current mainly passes through the graphite punches due to a high resistance at the interface between the graphite punches and graphite die. The current (*I*) induced Joule heat ($Q_J$) would act as the main heat source and heat the graphite punches. According to the Joule's law[20], the relationship between Joule heat and current as the below Expression (1):

$$Q_J = I^2 \cdot R \cdot t \tag{1}$$

where *R* is the resistance of the graphite punches and *t* is the action time of the current. Notably, a part of the Joule heat will be absorbed by the graphite die, the residual heat (*Q*) will result in a temperature change ($\Delta T$) in the graphite punches. From the specific heat equation[25]:

$$Q = C_p \cdot m \cdot \Delta T \tag{2}$$

where $C_p$ and *m* are the specific heat capacity and the weight of the punches, respectively. Based on the analysis from the Expression (1) and (2), it could be concluded that the temperature change is positively correlated with the current. Furthermore, the temperature change must cause the graphite punches to expand or shrink. In case of the SPS heating cycle, the temperature rise of the graphite punches would inevitably lead to its expansion (i.e., displacement change, $\Delta d$). For the graphite punches, its expansion can be simply recognized as a one-dimension expansion because the other two-dimensions were restricted by the graphite die. The displacement change in one-dimension can be estimated by the Expression (3)[26]:

$$\Delta d = d_0 \cdot \chi \cdot \Delta T \tag{3}$$

where $d_0$ is the original length of the graphite punches and $\chi$ is the linear expansion coefficient of the graphite punches under certain pressure. Therefore, the displacement change has a linear relationship with temperature change.

Fig. 6a shows the changes of the current, temperature and displacement as function of the sintering time for the empty graphite die. To clear describe and understand the Fig. 6a, the sintering process was artificially divided into four stages of

the stage Ⅰ (heating from room temperature to 600 °C), stage Ⅱ (holding at 600 °C for 5 min), stage Ⅲ (heating from 600 °C to 1500 °C) and stage Ⅳ (cooling from 1500 °C to room temperature). At the stage Ⅰ, the current-induced temperature change and temperature-induced displacement change are hard to clear because of the lower limit of temperature detection. But it can also be found that the current induced Joule heat results in a significant expansion on the graphite punches. Notably, the displacement and current curves show a rapid rising when the temperature rapid heating from 570 °C to 600 °C. This agree well with the relations among current, temperature and displacement based on the previous analysis of the Expression (1)-(3). Due to the temperature measuring position locates in the graphite die, the actual temperature of the graphite punches would be higher than the measured temperature of 600 °C. Therefore, there exist an obvious temperature overshoot at the initial moment of the stage Ⅱ. In order to maintain 600 °C, the current needs to be adjusted. At the last 2 min of the stage Ⅱ, the curve of displacement change has obvious turning point. This is owing to the pressure was evenly loaded from 10 MPa to 50 MPa as marked in Fig. 6a. More notably, a rapid increasing of the current can be found at the beginning of the stage Ⅲ when the temperature at a heating rate of 200 °C/min. The steep rising current aims at providing enough heat to ensure the heating rate of graphite die and punches. Nevertheless, the relations among current, temperature and displacement still coincide with the results of the previous analysis from the Expression (1) - (3). As the temperature above ~800 °C, the changing curves of current and displacement are tending to be stable. For the stage Ⅳ, the current was shut off and the blank system was cooling with furnace.

To clear the relationship between displacement changes of graphite punches and temperature changes in actual SPS conditions, the corresponding data at stage Ⅲ was chosen and showed in Fig. 6b. It can be found that the displacement increases

linearly with temperature, which conforms to the conclusion of the Expression (3). Notably, a slight abnormal change of the displacement when start heating at 600 °C, which would be owing to the steep rising current. To obtain a convinced data, the selection of temperature in Fig. 6b starts from 800 °C. Furthermore, the obvious densification of W-Cr-Zr alloyed powders at least start at 800 °C based on the later analysis. According to the Fig. 6b, the displacement of graphite punches depends on the temperature during SPS process can be calculated. After calculation, the slope (*k*) of the fitted line in Fig. 6b is approximately $1.70\times10^{-3}$ mm/°C. The expansion amount (displacement value) of graphite punches is approximately 1.3 mm, when it was heated from room temperature to 1500 °C under the current SPS conditions. This is a non-negligible value, means that the expansion of graphite punches must be considered when analyzing the displacement curve of the W-Cr-Zr alloyed powders during SPS process.

4.2 Densification process of W-Cr-Zr alloy

To clear the influence of heating rates on the densification process of W-Cr-Zr samples, the displacement change as function of the sintering time is showed in Fig. 7a. It can be found that the displacement curves contain three alternative expansion stages (ES Ⅰ, Ⅱ and Ⅲ) and shrinkage stages (SS Ⅰ, Ⅱ and Ⅲ) as marked in Fig. 7a. For the ES Ⅰ and SS Ⅰ, the displacement changes should be mainly attributed to the expansion and shrinkage of the graphite punches, which could be deduced from the displacement changes at stages Ⅰ and Ⅱ in Fig. 6a. There appear two significant shrinkage stages of SS Ⅱ and SS Ⅲ, which are owing to the fast densification of W-Cr-Zr alloyed powders and the shrinkage of the overall system at the cooling stage, respectively. The fast densification temperature of W-Cr-Zr alloyed powders almost starts from 800 °C and ends roughly at 1380 °C. Notably, there exists a slight thermal expansion (ES Ⅱ) between SS Ⅰ and SS Ⅱ, where before the significant densification. It should be owing to the expansion amount of graphite

punches higher than the shrinkage amount of the alloyed powder. When the temperature above ~1380 °C (as marked in Fig. 7a), a slowly rising in displacement can be observed (ES Ⅲ) and the magnified view was showed in Fig. 7b. It is obvious that the displacement increases linearly with temperature increasing under a specific heating rate. The corresponding slopes (*k*) are also noted in Fig. 7b. The values of these slopes show an upward trend with increasing the heating rate. When W-Cr-Zr sample sintered at a hating rate of 200 °C/min, the slope in Fig. 7b is $1.70\times10^{-3}$ mm/°C, which is equal to that of graphite (Fig. 6b). This may be owing to a low thermal expansion of W-Cr-Zr alloy during ES Ⅲ. Actually, the thermal expansion coefficient of the dense W-Cr-Zr bulk was examined and the corresponding value is approximately $7.5\times10^{-6}$ /°C under pressureless condition. Due to the sample height is approximately 5 mm after densification, the expansion amount of W-Cr-Zr alloy is approximately 4.5 $\times10^{-3}$ mm range from 1380 °C to 1500 °C, which is far less than that of graphite (approximately 0.20 mm). In addition, the actual elongation of W-Cr-Zr alloy should be more less because of an applied pressure (50 MPa) was loaded during the SPS densification process. Therefore, the rising in displacement during the ES Ⅲ is mainly owing to the expansion of graphite punches.

Furthermore, the densification process of W-Cr-Zr sample sintered with different heating rates can be also evaluated by the change curves of the relative density. The relative density changes of W-Cr-Zr samples during sintering should be depend on the changes in volume. Specifically, the volume of W-Cr-Zr sample during the SPS densification process depends on its height because its radial directions were restricted by the graphite die. The height of the sample can be obtained by subtracting the shrinkage amount from the original height of the sample ($H_0$ = 8.7 mm). During the SPS process, the shrinkage amount can be calculated by subtracting the expansion amount of graphite punches ($H_g$) from the corresponding displacement curves ($H_d$) of the samples. The instantaneous height ($H_i$) of sample can be confirmed by the

Expression (4):

$$\mathrm{H}_i = \mathrm{H}_0 + \mathrm{H}_d - \mathrm{H}_g \tag{4}$$

where $H_d$ is the value of displacement recorded by software system. The heat rate should influence on the value of $H_g$, it could be considered when calculating the instantaneous height of W-Cr-Zr samples during the SPS process. From the Fig. 6b and Fig. 7b, the slope of the displacement-temperature curve for the graphite punches is equal to the case for the W-Cr-Zr sample when performed at the same heating rate of 200 °C/min. Based the above discussion in Fig. 7b, the expansion behavior of graphite punches in SPS system with different heating rates can be evaluated by the corresponding slops in Fig. 7b. In addition, the instantaneous density ($\rho_i$) can be written as the below Expression (5)[27]:

$$\rho_i = \frac{\mathrm{H}_0}{\mathrm{H}_i}\rho_0 \tag{5}$$

where $\rho_0$ is the compact density of the W-Cr-Zr sample. The instantaneous relative density ($\rho_{Ri}$, %) could be calculated by the formula of $\rho_{Ri} = \frac{\rho_i}{\rho_T} \cdot 100\%$. From the foregoing discussion in Fig. 6a, an abnormal change in displacement is appeared when start heating from 600 °C because of the steep rising current. If W-Cr-Zr sample sintered at a higher heating rate, a steeper rising current would be yielded. For the convenience of analyzing the densification process, the selection of displacement values in Fig. 7a just starts from 800 °C. Fig. 7c shows the relative density of the W-Cr-Zr samples sintered with different heating rates as function of temperature. It can be found that the W-Cr-Zr alloys exhibit similar densification behaviors and the final relative density of the W-Cr-Zr samples are approximately 98.5%, which is equal to the measured value by Achimedes' principle. Furthermore, when these W-Cr-Zr samples reach up to the highest relative density, the corresponding temperature are about 1380 °C, as shown in Fig. 7c. This is the reason why the temperature of 1380 °C was used as the temperature boundary between the SS Ⅱ and the ES Ⅲ in Fig. 7a.

Nevertheless, it is hard to distinguish the influence of the heating rate on the densification process from the relative density curve of Fig. 7c. It is worth pointing that

different heating rate means different sintering time. Therefore, a concept of the instantaneous densification rate, i.e., the change rate of relative density per unit time, is used to reflect the influence of the heating rate on the densification process. The instantaneous densification rate ($\dot{\rho}$) can be calculated by[27]:

$$\dot{\rho} = \frac{d\rho_i}{dt_i} = \rho_0 H_0 \left(\frac{H_{i+1}-H_i}{H_{i+1}H_i(t_i-t_i)}\right) \quad (6)$$

The instantaneous densification rates of the W-Cr-Zr samples sintered with different heating rates as function of temperature is showed in Fig. 7d. It can be seen that the increase in heating rate leads to an increase in the instantaneous densification rate, which is consistent with the previously reported results[28,29]. The temperature of the maximum densification rate decreases with the heating rate increasing, and the corresponding temperature decrease from ~1300 °C to ~1250 °C. As mentioned above, the high heating rate requires high current under certain SPS conditions. Indicating that the current not only can reduce the activation energy of sintering and but also improve the densification behavior. It agrees the previous claims that the high current could reduce the activation energy of grain boundary diffusion and accelerate the densification kinetics[28]. In addition, the densification process of W-Cr-Zr samples are almost finished when the temperature reaches up to ~1380 °C (as marked in Fig. 7a and c).

4.3 Precipitation behavior of Cr

Homogeneous structure would be one essential positive factor for improving the oxidation resistance of SPTAs[15]. In this work, the completely alloyed powder should be an advantage for producing the homogenous structure of SPTAs by SPS technology at a low temperature. Notably, there exist two possible processes to realize the homogeneous structure during the SPS densification process. One possibility is that the STPAs directly inherits the characteristic of homogeneous structure from the powder. For the other possibility, the completely alloyed powder precipitates to form Cr-rich phases firstly and then becomes homogeneous structure of SPTAs in the follow sintering process. From the foregoing SEM images (Fig. 3) and XRD spectra (Fig. 4), W-Cr-Zr samples with homogenous structure or containing Cr-rich phases are

occurred when changing the heating rate. Fig. 8a shows the binary phase diagram of W-Cr alloy[23]. Finding that the solution temperature of W-11.4Cr binary system is approximately 1563 °C, which higher than the sintering temperature (1500 °C) of the W-11.4Cr-1.0Zr alloys in this study. Based on the W-Cr binary phase diagram, Cr precipitation should be inevitably in case of the current W-Cr-Zr system when the sintering temperature below solution temperature. However, the homogeneous structure of W-Cr-Zr alloy has been obtained as sintered 1500 °C with a high heating. It indicates that the formation of homogeneous SPTAs follows the other possibility, which is main conducted by the heating rate. Therefore, a thorough understanding the influence of heating rate on the Cr precipitation behavior is critical to obtaining the homogeneous structure of SPTAs.

From the Fig. 8a, it clear shows that the sintering temperature must higher than the solution temperature for obtaining a homogenous structure of SPTAs. It implies that the actual sintering temperature is not but higher than the designated/measured sintering temperature of 1500 °C. Fig. 8b shows the temperature changes of W-Cr-Zr samples sintered with different heating rates as function of sintering time. A slight temperature overshoot can be observed especially sintered at a high heating rate. To clarify the extent of the temperature overshoot in detail, Fig. 8c presents the relationship between the measured sintering temperature and the corresponding heating rate. It can be observed that the measured sintering temperature increases with the increase of heating rate, which would be attributed to the thermal inertia. As the sample sintered with a heating rate of 300 °C/min, the measured sintering temperature is approximately 1523 °C, which is still below the solution temperature. Notably, the measured temperature is not the actual temperature, therefore, the actual sintering temperature should be higher than the measured sintering temperature due to the distance and thermal loss from the samples to the “detection point”[29]. Zofia Trzaska et al. calibrated the temperature with Cu, founding that the temperature difference is approximately 27 °C when the heating rate is 20 °C/min[31]. In addition, the temperature difference may be larger, when the sintering temperature is higher or

the heating rate is faster. Based on the foregoing analysis, the actual sintering temperature could reach up to or even exceed its solution temperature and avoiding Cr precipitation during the SPS densification at a high heating rate.

4.4 Influence of current

During SPS densification process, the current passes through a conductive powder and generates Joule heat. The yielded heat would be benefit to the powder consolidation. Besides, several studies[32,33] reported that the applied current could carry high-momentum electrons and accelerate atomic migration, which would be the reasons that the SPS technology could promote sintering densification compared to HP technology. Fig. 9a presents the current evolutions of the W-Cr-Zr samples sintered with different heating rates as function of sintering time. It can be found that a higher heating rate requires a higher current and a higher heating rate means a shorter sintering time. In other words, a higher current would result in a higher densification rate as shown in Fig. 7d. This would be a reason why the W-Cr-Zr samples have a similar density (Fig. 7c). In addition, the heating rate would be benefit to the homogenization degree of W-Cr-Zr samples as analyzed from the Fig. 3 and Fig. 4. Therefore, the current could improve the homogenization process by enhancing atomic diffusion in case of W-Cr-Zr system.

Furthermore, it can be found that there exist obvious peaks broadening phenomenon in the XRD spectra (Fig. 4a). Generally, XRD peaks broadening should rely on the broadening from nano crystalline size and microstrain[34]. Assuming that the crystal of the sintered W-Cr-Zr samples with a characterization of isotropic nature, the Williamson-Hall equation[35] is given for evaluating the total peak broadening ($\beta_{hkl}$) as below:

$$\beta_{\mathrm{hkl}} = \beta_{\mathrm{S}} + \beta_{\mathrm{D}} \tag{7}$$

where $\beta_S$ and $\beta_D$ are the peak broadenings due to the microstrain and crystalline size, respectively. The microstrain induced peak broadening $\beta_S$ is given by[36]:

$$\beta_{\mathrm{S}} = 4\delta \tan \theta_{\mathrm{hkl}} \tag{8}$$

where $\delta$ is the microstrain, which mainly caused by dislocations and solute atoms ($\delta = \delta_d + \delta_s$) and $\theta_{hkl}$ is the diffraction angle of the corresponding crystal plane (*hkl*). In addition, the nano crystalline induced peak broadening $\beta_D$ can be given as[37]:

$$\beta_D = \frac{K\lambda}{\cos\theta_{hkl} D} \tag{9}$$

where *D and K* are the Scherrer's crystallite size and a constant (0.89), respectively. *λ* is the wavelength of the incident X-ray, which is 0.154056 nm for the Cu target. Based on the equations of (8) and (9), rearranging the Expression (7) as below:

$$\beta_{hkl} \cos\theta_{hkl} = \frac{K\lambda}{D} + 4\delta \sin\theta_{hkl} \tag{10}$$

Notably, it couldn't ignore the effect on peaks broadening induced by crystalline size if the crystalline size is less than 100 nm[38]. From the Fig.3 and Fig. 5c, the crystalline size of W-Cr-Zr samples sintered with different heating rates are approximately 500 nm, which is larger than 100 nm. Therefore, microstrain should be the main factor resulting in the XRD peaks broadening, which can be evaluated by the following equation:

$$\beta_{hkl} \cos\theta_{hkl} \approx 4\delta \sin\theta_{hkl} \tag{11}$$

Furthermore, $\beta_{hkl}$ consists of two parts of measured broadening ($\beta_m$) and instrumental broadening ($\beta_i$), and it can be calculated by the following relation:

$$\beta_{hkl} = \sqrt{\beta_m^2 - \beta_i^2} \tag{12}$$

where the $\beta_m$ can be confirmed form the XRD spectra. For the solid solution alloy of W-Cr-Zr, it must to consider the microstrain induced from the solute atoms. Therefore, $\beta_i$ was considered from the XRD spectrum of the undistorted pure W powder. Four crystal planes of (110), (200), (211) and (220) were used to evaluated the total peak broadening ($\beta_{hkl}$) of the W-Cr-Zr samples sintered with different heating rates. After calculation, a typical Williamson-Hall plot is drawn by taking $4\,sin\,\theta_{hkl}$ along x-*axis* and $\beta_{hkl}\,cos\,\theta_{hkl}$ along *y-axis* as shown in Fig. 9b. According to the equation (12), the corresponding points for each samples are fitted by the linear equations, which are marked with the corresponding color lines in Fig. 9b. The slopes of the fitted lines present the corresponding the microstrain ($\delta$) in W-Cr-Zr samples.

Fig. 9c shows the microstrain values of W-Cr-Zr samples, indicating that it decreases with the increase of the heating rate. When the W-Cr-Zr alloy sintered at a heating rate of 300 °C/min, the microstrain is only approximately $2.14\times10^{-3}$. As pointed earlier, the microstrain mainly relies on the microstrain induced from dislocations and solute atoms. From the foregoing SEM images (Fig. 3) and EDX results (Fig. 5a), the solubility of Cr in the W matrix increases with the heating rate increasing. It means that the microstrain ($\delta_s$) induced by the solute atoms increases gradually with the heating rate increasing. Combined to the Fig. 9c, indicating that the microstrain ($\delta_d$) induced by dislocation density decreases with the heating rate increasing. In other words, the decrease in dislocation density should be owing to the high current, which is consistent with previous reports in cases of powder and deformed metals[30,39]. It has reported that the high current could improve or accelerate the mobility of dislocations and lead to the annihilation of dislocation [40,41].

**5. Conclusions**

Self-passivating tungsten alloy of W-Cr-Zr system as a promising candidate material for the first wall in future fusion reactor was produced following powder metallurgy routes of mechanical alloying and continuous SPS densification. During the SPS densification process of W-Cr-Zr alloys, the influences of heating rate on densification process and microstructure evolution were evaluated to provide an in-depth understanding.

To clear the deification process of W-Cr-Zr samples, the expansion behavior of graphite punches was considered by performing a blank heating cycle on an empty graphite die. After analysis, founding that the temperature change is positively correlated with the current and the temperature change should be the directly factor that results in the expansion or shrinkage of graphite punches. Further, the relationship between displacement and temperature changes can be fitted by a linear equation when the temperature above ~800 °C, and the corresponding slope (*k*) is approximately $1.70\times10^{-3}$ mm/°C.

From the displacement curves, the densification process of W-Cr-Zr samples

contain three alternative expansion and shrinkage stages. The significant shrinkage stage, i.e., the obvious densification stage of W-Cr-Zr alloyed powders was occurred at a temperature range from ~800 °C to ~1380 °C. After considering the expansion behavior of graphite punches, the densification behaviors of W-Cr-Zr samples with different heating rates could be evaluated. With the temperature changes, W-Cr-Zr samples exhibit similar densification behaviors and the final relative density are approximately 98.5%. Notably, the corresponding instantaneous densification rate increase with the increase of heating rate.

Furthermore, W-Cr-Zr alloys with homogeneous structure can be achieved when sintered with a high heating rate. High heating rate means high thermal inertia that lead to the actual temperature of W-Cr-Zr alloys could approach or even exceed its solution temperature and contributes to avoiding Cr precipitation. In addition, higher heating rate requires a higher current. The current plays the key role in improvement the microstructure of W-Cr-Zr bulk system. It not only can improve the homogenization process by enhancing atomic diffusion, but also can improve or accelerate the mobility of dislocations and lead to the dislocation annihilation.

**Acknowledgements**

This work is supported by the National Magnetic Confinement Fusion Program (Grant No. 2014GB121001), National Natural Science Foundation of China (Grant No. 51574101), the Fundamental Research Funds for the Central Universities (Grant Nos. JZ2019HGTA0040, JZ2019HGBZ0113, PA2019GDZC0096), the Foreign Science and Technology Cooperation Project of Anhui Province (Grant No. 201904b11020034), the Natural Science Foundation of Anhui Province (Grant No. 1908085ME115), the 111 Project (Grant No. B18018), the International Postdoctoral Exchange Fellowship Program of Helmholtz-OCPC (No. 20191015) and the Open Foundation of Key Laboratory of E&M (Zhejiang University of Technology), Ministry of Education & Zhejiang Province (EM2018120105).

**References**

[1] G. Federici, A. Zhitlukin, N. Arkhipov, R. Giniyatulin, N. Klimov, I. Landman, V.

Podkovyrov, V. Safronov, A. Loarte, M. Merola. Effects of ELMs and disruptions on ITER divertor armour materials, J. Nucl. Mater. 337–339 (2005) 684–690.

[2] J. Davis, V. Barabash, A. Makhankov, L. Plöchl, K. Slattery. Assessment of tungsten for use in the ITER plasma facing components, J. Nucl. Mater. 258–263 (1998) 308–312.

[3] D. Maisonnier, I. Cook, S. Pierre, B. Lorenzo, D.P. Luigi, G. Luciano, N. Prachai, P. Aldo, PPCS Team. DEMO and fusion power plant conceptual studies in Europe, Fusion Eng. Des. 81 (2006) 1123–1130.

[4] T. Wegener, F. Klein, A. Litnovsky, M. Rasinski, J. Brinkmann, F. Koch, C. Linsmeier. Development of yttrium-containing self-passivating tungsten alloys for future fusion power plants, Nucl Mate Energy. 9 (2016) 394–398.

[5] T. Wegener, F. Klein, A. Litnovsky, M Rasinski, J Brinkmann, F Koch, Ch Linsmeier. Development and analyses of self-passivating tungsten alloys for DEMO accidental conditions, Fusion Eng. Des. 124 (C) (2017) 183–186.

[6] A. Calvo, C. García-Rosales, F. Koch, N. Ordás, I. Iturriza, H. Greuner, G. Pintsuk, C. Sarbu. Manufacturing and testing of self-passivating tungsten alloys of different composition, Nucl Mate Energy. 9 (2016) 422–429.

[7] F. Koch, J. Brinkmann, S. Lindig, T. P. Mishra, Ch. Linsmeier. Oxidation behaviour of silicon-free tungsten alloys for use as the first wall material, Phys Scripta. 145 (2011) 014-019.

[8] T. Wegener, F. Klein, A. Litnovsky, M. Rasinski, J. Brinkmann, F. Koch, Ch. Linsmeier. Development of yttrium-containing self-passivating tungsten alloys for future fusion power plants, Nucl Mate Energy. 9 (2016) 394-398.

[9] F. Koch, H. Bolt. Self passivating W-based alloys as plasma facing material for nuclear fusion, Phys Scripta. T128 (2007) 100–105.

[10] X.Y. Tan, F. Klein, A. Litnovsky, T. Wegener, J. Schmitz, Ch. Linsmeier, J.W. Coenen, U. Breuer, M. Rasinski, P. Li, L.M. Luo, Y.C. Wu. Evaluation of the high temperature oxidation of W-Cr-Zr self-passivating alloys, Corros Sci. 147 (2019) 201–211.

[11] A. Calvoa, K. Schlueterc, E. Tejado, G. Pintsuk, N. Ordás, I. Iturriza, R. Neu, J.Y. Pastor, C. García-Rosales. Self-passivating tungsten alloys of the system W-Cr-Y for high temperature applications, Int. J. Refract. Met. H. 73 (2018) 29–37.

[12] P. López-Ruiz, N. Ordás, I. Iturriza, M. Walter, E. Gaganidze, S. Lindig, F. Koch, C. García-Rosales. Powder metallurgical processing of self-passivating tungsten alloys for fusion first wall application, J. Nucl. Mater. 442 (2013) S219–S224.

[13] Q.Q. Hou, K. Huang, L.M. Luo, X.Y. Tan, X. Zan, Q. Xu, X.Y. Zhu, Y.C. Wu. Microstructure and its high temperature oxidation behavior of W-Cr alloys prepared by spark plasma sintering, Materialia, 6 (2019) 100332.

[14] W. Liu, J. Di, L.H Xue, H.P Li, Y. Oya, Y.W. Yan. Phase evolution progress and properties of W-Si composites prepared by spark plasma sintering, J. Alloy Compd. 766 (2018) 739-747.

[15] A. Litnovsky, T. Wegener, F. Klein, Ch. Linsmeier, M. Rasinski, A. Kreter, X.Y. Tan, J. Schmitz, J. W. Coenen, Y.R. Mao, J. Gonzalez-Julian, M. Bram. New oxidation-resistant tungsten alloys for use in the nuclear fusion reactors, Phys Scripta. T170 (2017) 014012 (8pp).

[16] A. Calvo, C. García-Rosales, N. Ordás, I. Iturriza, K. Schlueter, F. Koch, G. Pintsuk, E. Tejado, J. Ygnacio Pastor. Self-passivating W-Cr-Y alloys: Characterization and testing, Fusion Eng. Des. 124 (2017) 1118-1121.

[17] J. Narayan. A new mechanism for field-assisted processing and flash sintering of materials, Scripta Mate. 69 (2013) 107–111.

[18] F. Balima, A. Largeteau. Phase transformation of alumina induced by high pressure spark plasma sintering (HP-SPS), Scripta Mater. 158 (2019) 20–23.

[19] B.Q Li, Z.L Yang, J.P Jia, Y. Zhong, X.X Liu, P.C Zhang, R. Gao, T. Liu, R. Li, H.W Huang, M.Z Sun, D.D.M Zhao. High temperature thermal physical performance of BeO/UO2 composites prepared by spark plasma sintering (SPS), Scripta Mater. 142 (2018) 70–73.

[20] N. Chawake, L.D. Pinto, A.K. Srivastav, K. Akkiraju, B.S. Murty, R.S. Kottad. On Joule heating during spark plasma sintering of metal powders, Scripta Mater. 93

(2014) 52-55.

[21] G. Lee, E.A. Olevsky, C. Maniere, A. Maximenko, O. Izhvanov, C. Back, J. McKittrick. Effect of electric current on densification behavior of conductive ceramic powders consolidated by spark plasma sintering, Acta Mater. 144 (2018) 524-533.

[22] M. Vilémová, F. Lukáč, J. Veverka, K. Illková, J. Matějíček. Controlling the carbide formation and chromium depletion in W-Cr alloy during field assisted sintering, Int. J. Refract. Met. H.79 (2019) 217–223.

[23] K. Frisk, P. Gustafson. An assessment of the chromium-molybdenum-tungsten system, Calphad. 12(3) (1988) 247-254.

[24] A.K. Srivastav, N. Chawake, D. Yadav, N.S. Karthiselva, B.S. Murty. Localized pore evolution assisted densification during spark plasma sintering of nanocrystalline W-5wt.%Mo alloy, Scripta Mate. 159 (2019) 41–45.

[25] Z.H. Xu, G.Y. Tang, S.Q. Tian, J.C. He. Research on the engineering application of multiple pulses treatment for recrystallization of fine copper wire, Mater Sci Eng A. 424(1-2) (2006) 300-306.

[26] Z. Pluta, T. Hryniewicz. Thermal expansion of solids, Int J Mod Phys. 3 (2012) 793-802.

[27] L. H. Liu, C. Yang, Y. G. Yao, F. Wang, W. W. Zhang, Y. Long, Y. Y. Li. Densification mechanism of Ti-based metallic glass powders during spark plasma sintering, Intermetallics. 66 (2015) 1–7.

[28] T. Paul, S.P. Harimkar. Viscous flow activation energy adaptation by isochronal spark plasma sintering, Scripta Mater. 126 (2017) 37-40.

[29] C. Yang, M. D. Zhu, X. Luo, L.H. Liu, W.W. Zhang, Y. Long, Z.Y. Xiao, Z.Q. Fu, L.C. Zhang, E.J. Lavernia. Influence of powder properties on densification mechanism during spark plasma sintering, Scripta Mater. 139 (2017) 96–99.

[30] S. H. Deng, R. D. Li, T. C Yuan, S. Y. Xie, M. Zhang, K. C. Zhou, P. Cao. Direct current-enhanced densification kinetics during spark plasma sintering of tungsten powder, Scripta Mater. 143 (2018) 25–29.

[31] Z. Trzaska, G. Bonnefont, G. Fantozzi, et al. Comparison of densification kinetics of a TiAl powder by spark plasma sintering and hot pressing, Acta Mater. 2017, 135:1-13.

[32] C.L. Liang, K.L. Lin. The microstructure and property variations of metals induced by electric current treatment: A review, Mate Charact. 145 (2018) 545–555.

[33] S.H. Deng, T.C Yuan, R.D. Li, M. Zhang, S.Y. Xie, M.B. Wang, L.B. Li, J.W. Yuan, Q.G. Weng. Influence of electric current on interdiffusion kinetics of W-Ti system during spark plasma sintering, International Journal of Refractory Metals & Hard Materials, 75 (2018) 184–190.

[34] K. Venkateswarlu, M. Sandhyarani, T.A. Nellaippan, N. Rameshbabu, Estimation of crystallite size, lattice strain and dislocation density of nanocrystalline carbonate substituted hydroxyapatite by X-ray peak variance analysis, Procedia Mater. Sci. (2014) 212–221.

[35] G.K. Williamson, R.E. Smallman. Dislocation densities in some annealed and cold-worked metals from measurements on the X-ray Debye-Scherrer spectrum, Philos Mag. 1 (1955) 34-46.

[36] K. Venkateswarlu, A.C. Bose, N. Rameshbabu. X-ray peak broadening studies of nanocrystalline hydroxyapatite by Williamson–Hall analysis, Physica B. 405(20) (2010) 4256-4261.

[37] R. Jenkins, J.L. de Varies, Worked Examples in X-ray Analysis, Macmillan, New York. pp (1978) 132–133.

[38] C.E. Kril, R. Birringer. Estimating grain-size distributions in nanocrystalline materials from X-ray diffraction profile analysis, Philos Mag. 77(3) (1998) 621-640.

[39] D. Fabre`gue, B. Mouawad, C.R. Hutchinson. Enhanced recovery and recrystallization of metals due to an applied current, Scripta Mater. 92 (2014) 3–6

[40] V. E. Gromov, L. I. Gurevich, V. A. Kuznetsov, T. V. Erilova, Czechoslov. Influence of electric current pulses on the mobility and multiplication of dislocations in Zn-monocrystals, Czech J Phys. 40 (8) (1990) 895–902.

[41] K. Liu, X. H. Dong, H. Y. Xie, F. Peng. Effect of pulsed current on the deformation

behavior of AZ31B magnesium alloy, Mater. Sci. Eng. A. 623 (2015) 97–103.

## Table

Table1 Several basic information of W-Cr based alloys produced by SPS technique.

| Material system | Sintering temperature (°C) | Heating rate (°C/min) | Holding time (min) | Relative density (%) | Phase composition |
|---|---|---|---|---|---|
| W-10.0Cr[13] | 1400 | \ | \ | 95.4 | Double phases |
| W-11.4Cr-0.6Y[15] | 1460 | 200 | 0 | 99.6 | Single phase |
| W-11.4Cr-0.6Y[15] | 1550 | 200 | 1 | 99.6 | Single phase |
| W-10Cr-1.0Hf[22] | 1750 | 100 | 3 | \ | Single phase |

## Figures captions

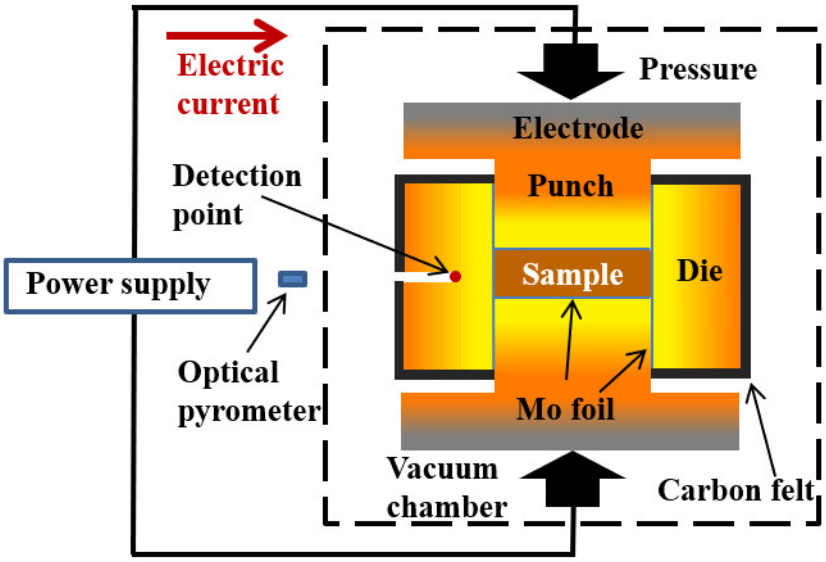


Fig.1. The combination schematic diagram of sintered bulk and graphite die in SPS facility.

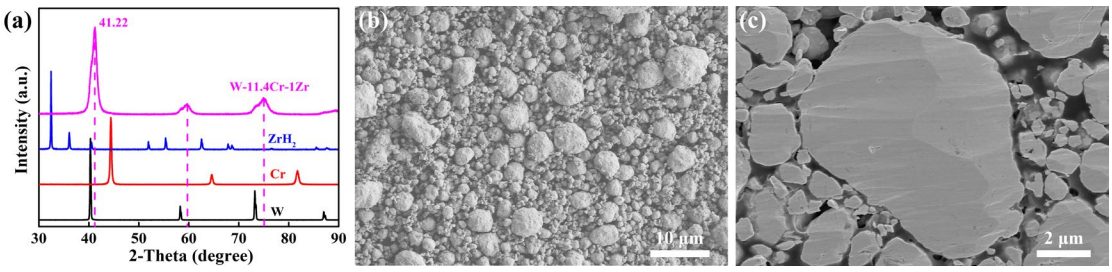


Fig.2. (a) XRD spectra of the raw powders and the W-Cr-Zr milled powders; SEM images of (b) the W-Cr-Zr milled powder and (c) their cross-section.

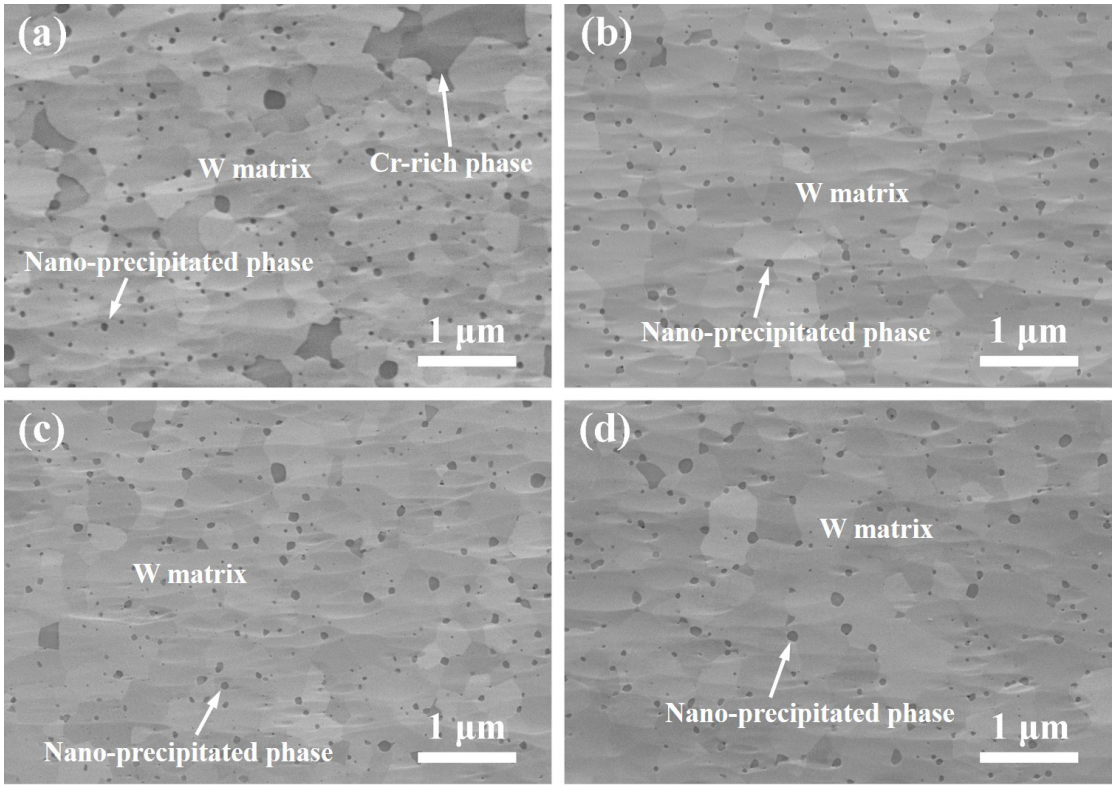


Fig.3. Microstructures of W-Cr-Zr samples sintered at 1500 °C with different heating rates (a) 50 °C/min; (b) 100 °C/min; (c) 200 °C/min; (d) 300 °C/min.

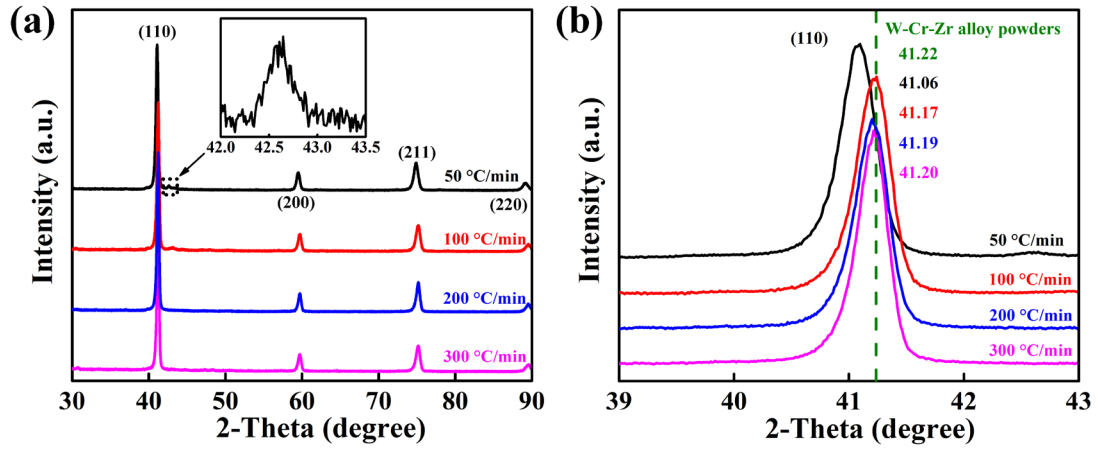


Fig.4. (a) XRD patterns of the W-Cr-Zr samples sintered at 1500 °C with different heating rates; (b) the magnified view of the diffraction peak (110).

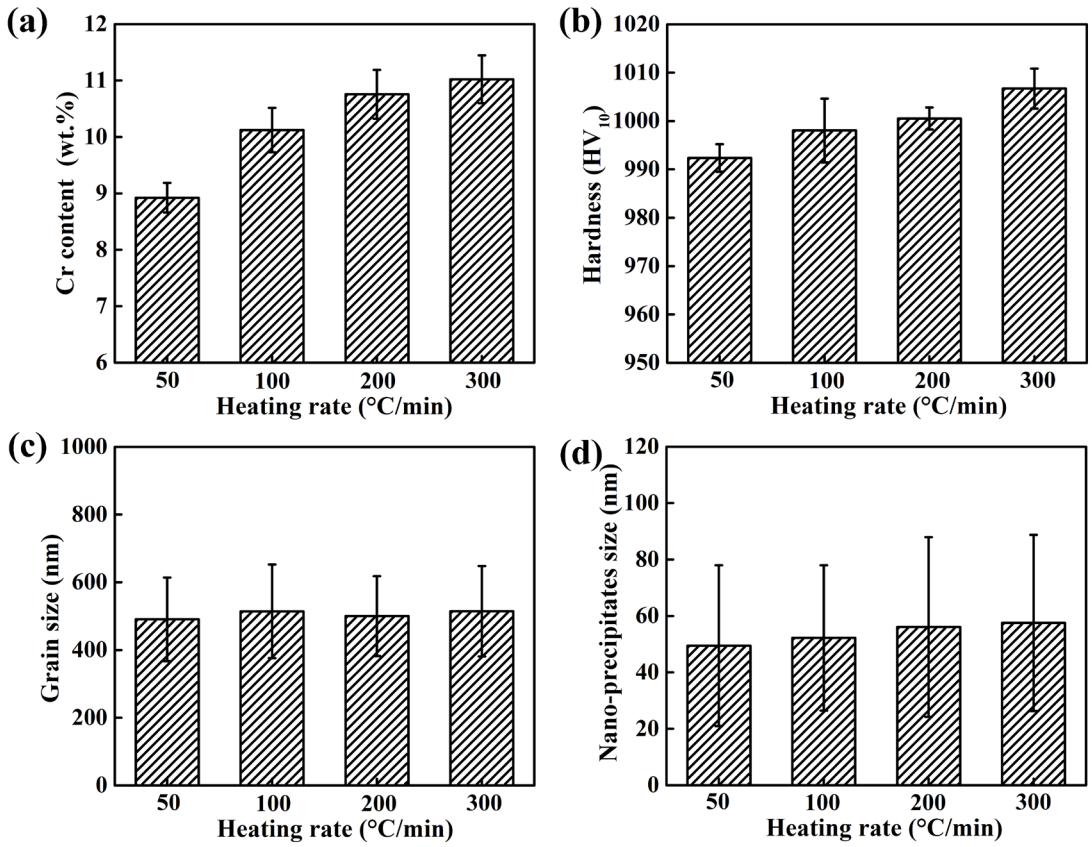


Fig.5. W-Cr-Zr samples sintered at 1500 °C with different heating rates (a) Cr content in the W matrix; (b) hardness; (c) grain size of the W-matrix; (d) the dimension of the nano-precipitates.

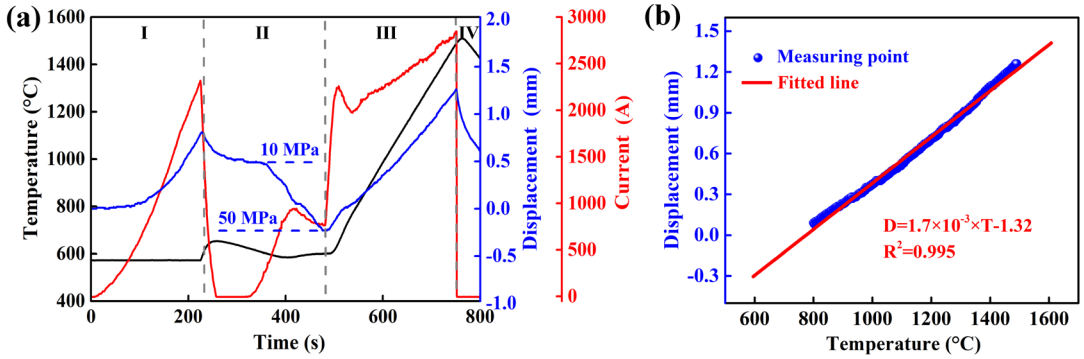


Fig.6. (a) The changes of the current, temperature and displacement as function of the sintering time for the empty graphite die heated up to 1500 °C with a heating rate of 200 °C/min; (b) the displacement curve at a temperature range of 800 °C -1500 °C and the corresponding fitted red line.

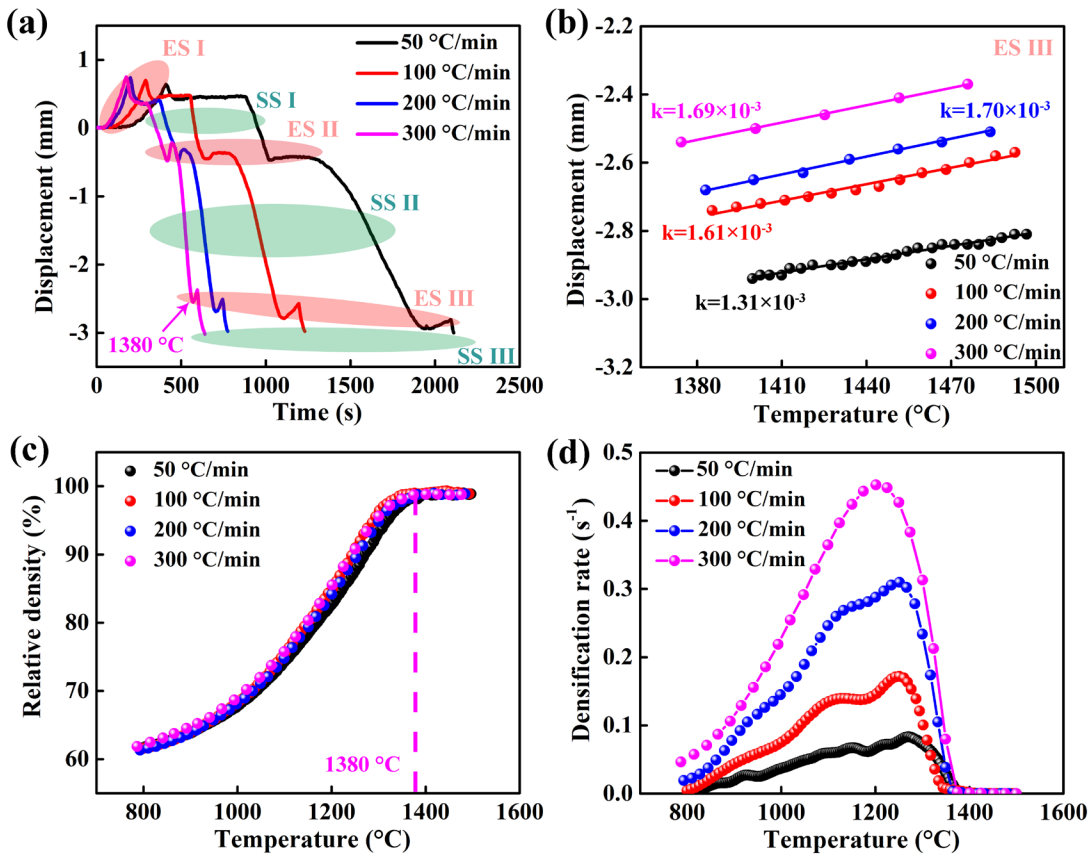


Fig.7. (a) The displacement changes of W-Cr-Zr samples as function of sintering time; (b) the displacement-temperature curves of the ES Ⅲ; (c) the densification curves of W-Cr-Zr samples; (d) instantaneous densification rate of W-Cr-Zr samples at a temperature range of 800 °C -1500 °C.

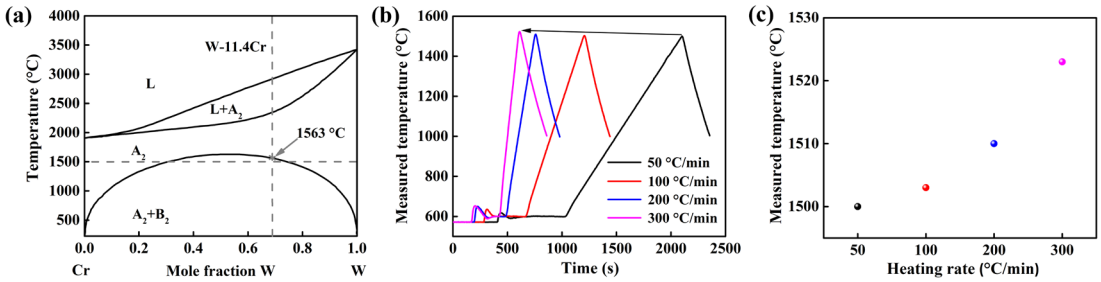


Fig.8. (a) W-Cr binary phase diagram[23]; (b) the measured temperature of W-Cr-Zr samples as function of sintering time; (c) the relationship between measured sintering temperature and heating rates.

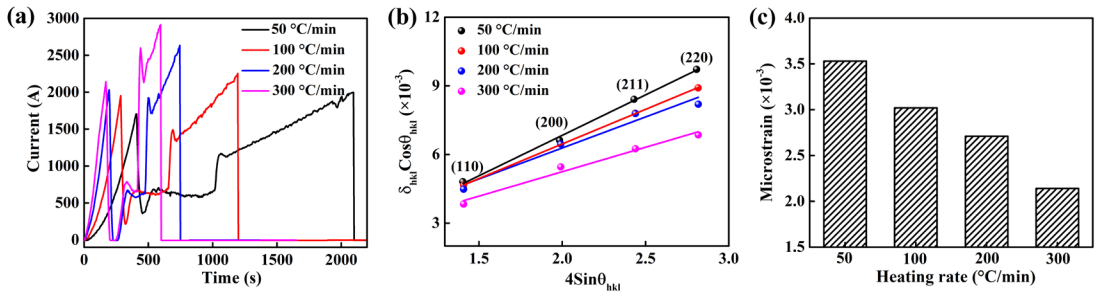


Fig.9. (a) The current evolutions of W-Cr-Zr samples as function of sintering time; (b) the typical Williamson-Hall plots of the W-Cr-Zr samples; (c) the microstrain values determined from the Williamson-Hall plots versus heating rates.